PHYSICAL REVIEW B **95**, 245414 (2017)

Gate-dependent spin Hall induced nonlocal resistance and the symmetry of spin-orbit scattering in Au-clustered graphene

Jungmin Park, Hyung Duk Yun, Mi-Jin Jin, Junhyeon Jo, Inseon Oh, Vijayakumar Modepalli,
Soon-Yong Kwon, and Jung-Woo Yoo[*]
School of Materials Science and Engineering-Low Dimensional Carbon Materials Center, Ulsan National Institute of Science and Technology, Ulsan, 44919, Republic of Korea

(Received 27 November 2016; revised manuscript received 4 May 2017; published 14 June 2017)

Engineering the electron dispersion of graphene to be spin-dependent is crucial for the realization of spin-based logic devices. Enhancing spin-orbit coupling in graphene can induce spin Hall effect, which can be adapted to generate or detect a spin current without a ferromagnet. Recently, both chemically and physically decorated graphenes have shown to exhibit large nonlocal resistance via the spin Hall and its inverse effects. However, these nonlocal transport results have raised critical debates due to the absence of field dependent Hanle curve in subsequent studies. Here, we introduce Au clusters on graphene to enhance spin-orbit coupling and employ a nonlocal geometry to study the spin Hall induced nonlocal resistance. Our results show that the nonlocal resistance highly depends on the applied gate voltage due to various current channels. However, the spin Hall induced nonlocal resistance becomes dominant at a particular carrier concentration, which is further confirmed through Hanle curves. The obtained spin Hall angle is as high as ~0.09 at 2 K. Temperature dependence of spin relaxation time is governed by the symmetry of spin-orbit coupling, which also depends on the gate voltage: asymmetric near the charge neutral point and symmetric at high carrier concentration. These results inspire an effective method for generating spin currents in graphene and provide important insights for the spin Hall effect as well as the symmetry of spin scattering in physically decorated graphene.

DOI: 10.1103/PhysRevB.95.245414

I. INTRODUCTION

Graphene is a two-dimensional honeycomb crystal with an atomic AB site symmetry, which yields a linear dispersion around the K and K' points with a chirality for the quasiparticle's isospin [1,2]. The sublattice asymmetry when patching graphene with a hexagonal boron nitride can cause a Berry curvature, leading to the separation of isospins via the valley Hall effect [3]. While the isospin quantum number adds another dimension, the manipulation of the real spin of an electron in graphene remains as a frontier of spintronics [4–6]. A mandatory requirement for exploiting electron spins in graphene is the facile control of spin-orbit coupling (SOC). Instilling SOC into graphene allows splitting and detecting electron spins via the spin Hall effect (SHE) and its inverse effect [7,8]. In addition, SOC arisen from broken inversion symmetry, i.e., Rashba SOC, allows a gate controllable spin precession [9,10]. The original Datta-Das concept of the spin-field-effect transistor (spin-FET) can be achieved only through a channel with an exceptionally long mean free path [11–13]. Developing practical methods for enhancing SOC in graphene will make it an ideal material at the forefront of spintronics.

Thus far, several methods have been explored to enhance SOC in graphene. For example, chemisorbed hydrogen and fluorine atoms in graphene have been predicted to induce strong SOC (~10 meV) through the distortion of its planar structure via sp^3 hybridization [14,15]. Further, theoretical calculations determined that physically decorated adatoms in graphene could also induce strong SOC without breaking sp^2 hybridization and the sublattice symmetry [16,17]. In particular, Au intercalation at the graphene/Ni interface can cause a giant spin-orbit splitting as large as ~100 meV near the Dirac point [18]. Recently, Balakrishnan *et al.* reported SHE induced nonlocal resistances ($R_{\mathrm{NL}}^{\mathrm{SHE}}$s) in hydrogenated chemical vapor deposition (CVD) and physically decorated graphene in sequence [8,19]. They showed a large symmetric $R_{\mathrm{NL}}^{\mathrm{SHE}}$ peak near the charge neutral peak, which displayed a field dependent precession signature (i.e., a Hanle curve). The appearance of a large R_{NL} peak itself often was attributed to the presence of SHE in graphene [20]. However, these nonlocal transport results have raised critical debates [21–23]. Wang *et al.* reported that large nonlocal resistances (R_{NL}s) were observed in Au- or Ir-decorated graphenes, but no evidence of Hanle signature was detected [22]. Kaverzin and van Wees also reported the absence of the field-induced effect in R_{NL} for hydrogenated graphene and questioned the origin of previously reported $R_{\mathrm{NL}}^{\mathrm{SHE}}$ [23]. Further, a recent theoretical study showed the presence of a large R_{NL} in Au-decorated graphene even in the absence of SOC [24]. They also reported that the spin Hall angle (θ_{SH}) in Au-clustered graphene can significantly fluctuate according to the applied gate voltage [24].

Here, we report gate-dependent $R_{\mathrm{NL}}^{\mathrm{SHE}}$ in Au-clustered graphene. A Hall-bar-like (H-bar) geometry is employed to generate a transverse spin-polarized current via the SHE, which in turn can be detected owing to the inverse SHE. A significant gate-dependent fluctuation in R_{NL} is observed at low temperature. However, $R_{\mathrm{NL}}^{\mathrm{SHE}}$ becomes dominant at a particular carrier concentration, where the Hanle curves are consistently observed at various temperatures. The temperature dependence of the spin relaxation time (τ_s) suggests that the Elliot-Yafet (EY) mechanism prevails at that specific carrier concentration. Further study on magnetoconductance (MC) reveals that asymmetric spin-orbit scattering (SOS) prevails near the charge neutral point, while symmetric SOS

---

[*] jwyoo@unist.ac.kr

dominates at a higher carrier concentration. These results provide an alternative approach for effective spin-charge conversion in graphene and important insights for $R_{\mathrm{NL}}^{\mathrm{SHE}}$ as well as the symmetry of SOS therein.

Our paper is organized as follows. In Sec. II, we describe the details of experimental methods, including device fabrication and characterization. In Sec. III, we discuss our results starting from the behavior of nonlocal resistance in our Au-clustered graphene and then show how we determined gate-dependent SHE induced nonlocal resistance. We then discuss behavior of MC in Au-clustered graphene, which displays a gate-dependent variation on the symmetry of SOC. Finally, Sec. IV provides the conclusion.

II. EXPERIMENTAL METHODS

Graphene used for our device was grown on a polycrystalline Cu foil using a chemical vapor deposition method demonstrated elsewhere [25]. A 25 μm copper foil (Alfa Aesar, 99.8% purity) was electropolished in phosphoric acid for 15 min and rinsed with distilled water and isopropyl alcohol (IPA). The copper foil was loaded into a quartz tube three-zone furnace, and the temperature was increased to 1050 °C in the H_2 environment for the removal of native oxides in the copper with the surface reconstruction. Graphene was synthesized by introducing CH_4 gas and H_2 gas with a ratio of 10:5 (sccm) for 15 min and transferred onto the SiO_2 (300 nm)/p-Si subatrate using a polymethyl methacrylate (PMMA) wet transfer process. Then, the sample was annealed in high vacuum at 300 °C in order to remove possible resist residues. The devices were fabricated by employing the electron beam lithography. Thermally deposited Au (60 nm)/Cr (3 nm) layers were used for electrodes. A Hall bar geometry of the nonlocal graphene device was defined by using the oxygen plasma etching. An ultrathin Au layer (∼1 nm) was deposited by the thermal evaporation. Prior to the measurements, the fabricated devices were annealed in N_2/H_2 gas at 300 °C to remove residual resists. Electrical measurements were performed in a Quantum Design Physical Property Measurement System (PPMS). Indium with a copper wire was used for the electrical contacts to Au pads of the device. The four-terminal nonlocal measurements were performed by using a Keithley source meter (K2636) and a nanovoltmeter (K2182). Gate voltage was applied through the contact to the bottom of SiO_2 (300 nm)/p-Si substrate. X-ray photoelectron spectroscopy (XPS) was performed by employing a Thermo Scientific spectrometer (K-Alpha) with a monochromatic Al Kα x-ray source (1486.6 eV). The spot size of the incident x ray was 400 μm in diameter. Alpha 300R spectrometer (WITec) with a 532 nm laser source was used for the Raman spectroscopy.

III. RESULTS AND DISCUSSION

A. Nonlocal resistance in Au-clustered graphene

Figure 1(a) shows a schematic of the nonlocal graphene device in order to study $R_{\mathrm{NL}}^{\mathrm{SHE}}$. In the presence of SOC, a charge current flowing across the vertical line of the H bar generates a transverse spin current through the central channel line via the direct SHE. If the spin current persists through the channel, it can produce the nonlocal voltage via the inverse SHE. In fact, we have studied this nonlocal geometry device for a series of CVD, Au-decorated (0.05–0.2 nm deposition of Au), and Au-clustered graphene (1 nm deposition of Au) in order to investigate $R_{\mathrm{NL}}^{\mathrm{SHE}}$. All devices displayed large R_{NL} signal. However, other than Au-clustered graphene, we were not able to detect field-dependent Hanle curve, similar to the reports in Refs. [21–23]. Thus, we discuss results only from the Au-clustered graphene device in this paper. Figure 1(b) displays a scanning electron microscopy (SEM) image of the fabricated Au-clustered graphene device A with a channel width (w) of 1 μm and lengths (Ls) of 2, 3, and 4 μm. The thermally deposited ultrathin Au layer (∼1 nm) formed randomly distributed Au clusters with typical size of the order of 10 nm, as shown in enlarged Fig. 1(b). The determined Au coverage based on SEM image is ∼41.92% (see Supplemental Material [26]). The CVD graphene used in our device was a monolayer, as confirmed by its Raman spectrum (see Supplemental Material [26]). The XPS result showed that Au atoms did not form chemical bonds with the carbon atoms of graphene (see Supplemental Material [26]). Figure 1(c) displays ambipolar field-effect behavior at 300 K using the back gate. The upper x axis displays the estimated carrier concentration. This FET characteristic is nearly similar to that observed in a typical graphene FET, indicating that charge carriers mainly transport through the graphene layer. The gate voltage of the maximum resistivity, a charge neutral point, is located at around 5 V. The estimated mobility at the neutral point is $\sim 1000\ \mathrm{cm}^2/\mathrm{Vs}$ at 300 K. The rounding of a maximum resistivity region and the decrease in mobility of the Au-clustered graphene compared to that of the as-grown CVD graphene imply that the Au clusters introduces considerable charged impurity scatterings [27]. Typical resistivities of Au-clustered graphene devices near the charge neutral point were ∼5 kΩ, with slight sample to sample variation. These resistivity values were nearly similar to that of our as-grown CVD graphene. Both ambipolar field-effect behavior and the estimated resistivity suggest the charge carriers in our Au-clustered graphene devices mainly transport through the graphene.

Figure 1(d) displays a gate-dependent R_{NL} measured at 300 K for $L/w = 2,3,$ and 4 channels of device A. Similar to the local FET curve, R_{NL} for all channels of device A displayed maximum value near the charge neutral point. The dashed line in Fig. 1(c) is the simulated nonlocal Ohmic resistance ($R_{\mathrm{NL}}^{\mathrm{Ohm}}$), which is given as $R_{\mathrm{NL}}^{\mathrm{Ohm}} = \rho \exp(-\pi L/w)$, where ρ is the resistivity of the material [28]. The observed R_{NL} for all channels ($L/w = 2,3,$ and 4) were much higher than the $R_{\mathrm{NL}}^{\mathrm{Ohm}}$. Similar to previous reports [22,23], this unidentified large R_{NL} does not display an in-plane field-dependent spin precession signature.

In general, R_{NL} in the H-bar geometry of a graphene device can arise from various mechanisms. The total R_{NL} can be expressed as $R_{\mathrm{NL}} = R_{\mathrm{NL}}^{\mathrm{SHE}} + R_{\mathrm{NL}}^{\mathrm{Ohm}} + R_{\mathrm{NL}}^{\mathrm{Zeeman}} + R_{\mathrm{NL}}^{\mathrm{Valley}} + R_{\mathrm{NL}}^{\mathrm{Thermal}} + R_{\mathrm{NL}}^{\mathrm{Ballistic}} + \ldots$ Here, $R_{\mathrm{NL}}^{\mathrm{Ohm}}$ can be significantly reduced as long as $L/w \geqslant 3$. In the presence of a perpendicular magnetic field, Zeeman splitting separates electron and hole with opposite spins near the Dirac point leading to giant $R_{\mathrm{NL}}^{\mathrm{Zeeman}}$ [29]. The valley Hall effect due to global AB asymmetry can produce $R_{\mathrm{NL}}^{\mathrm{Valley}}$ [3]. $R_{\mathrm{NL}}^{\mathrm{Ballistic}}$

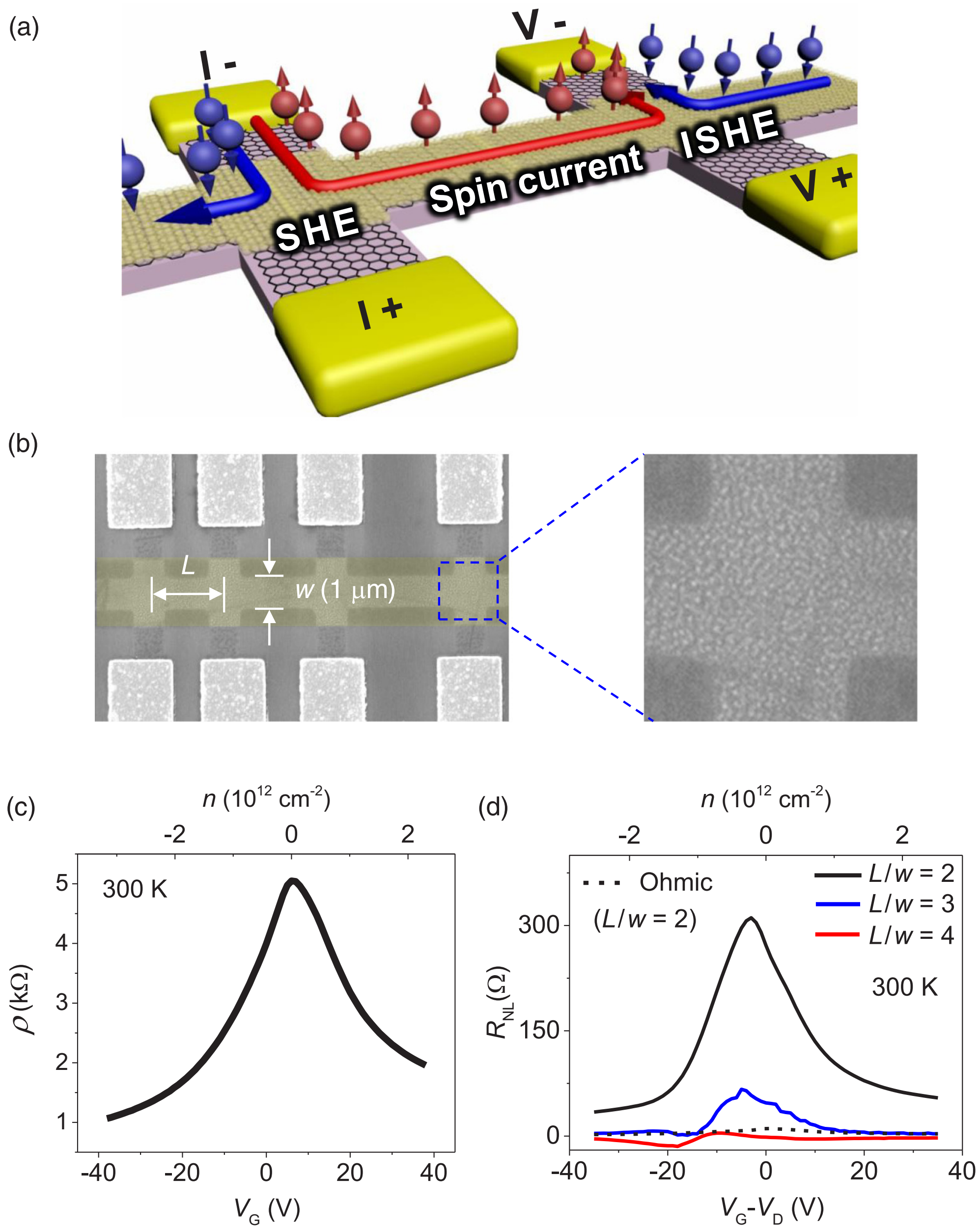

FIG. 1. Nonlocal device geometry and R_{NL} measured for device A. (a) Schematic of the H-bar geometry of the graphene device. (b) A SEM image of a graphene H-bar device. Randomly distributed Au clusters can be observed on an enlarged figure at the right panel. The determined Au coverage based on SEM image is ∼41.92%. (c) Gate-dependent local resistance of the Au-clustered device A displaying ambipolar field effect behavior. (d) R_{NL} as a function of applied gate voltage for different L/w ratios of device A at 300 K.

can produce negative resistance in the ballistic limit, i.e., $\lambda_e \gg w$ (where λ_e is the electron mean free path) [28]. The estimated λ_e values of our devices were typically less than 100 nm. Nonetheless, theoretical and experimental studies suggested that the nonlocal resistance could produce negative signal even in the quasiballistic limit of $\lambda_e < w$ [24,28]. Thus, the relevant contributions in our experiment are $R_{\mathrm{NL}}^{\mathrm{SHE}}$, $R_{\mathrm{NL}}^{\mathrm{Ballistic}}$, $R_{\mathrm{NL}}^{\mathrm{Thermal}}$, and other nonintuitive channels. Especially, the observed large positive R_{NL} in $L/w = 2$ and 3 might be associated with unidentified channels, as suggested in previous experimental reports [23]. Suppression of this nonintuitive R_{NL} as well as $R_{\mathrm{NL}}^{\mathrm{Ballistic}}$ could be achieved by increasing L/w.

In order to strongly suppress the unidentified nonlocal signal, we further increased L/w. Figure 2(a) displays the local FET characteristics measured for the Au-clustered device B, which has $L/w = 5.6$. The inset in Fig. 2(a) displays a SEM image of device B. The charge neutral point for device B is located at around 33 V. The estimated mobility near the neutral point is ∼1000 cm^2/Vs at 300 K. Figure 2(b) displays the gate-dependent R_{NL} measured at 300 K, The maximum positive R_{NL} is located near the Dirac region. The blue line in Fig. 2(b) indicates the simulated $R_{\mathrm{NL}}^{\mathrm{Ohm}}$. Note that the previously reported $R_{\mathrm{NL}}^{\mathrm{SHE}}$ exhibited a large symmetry peak around the Dirac point [8,19]. However, the observed R_{NL} in our device displays something similar to the derivative of the

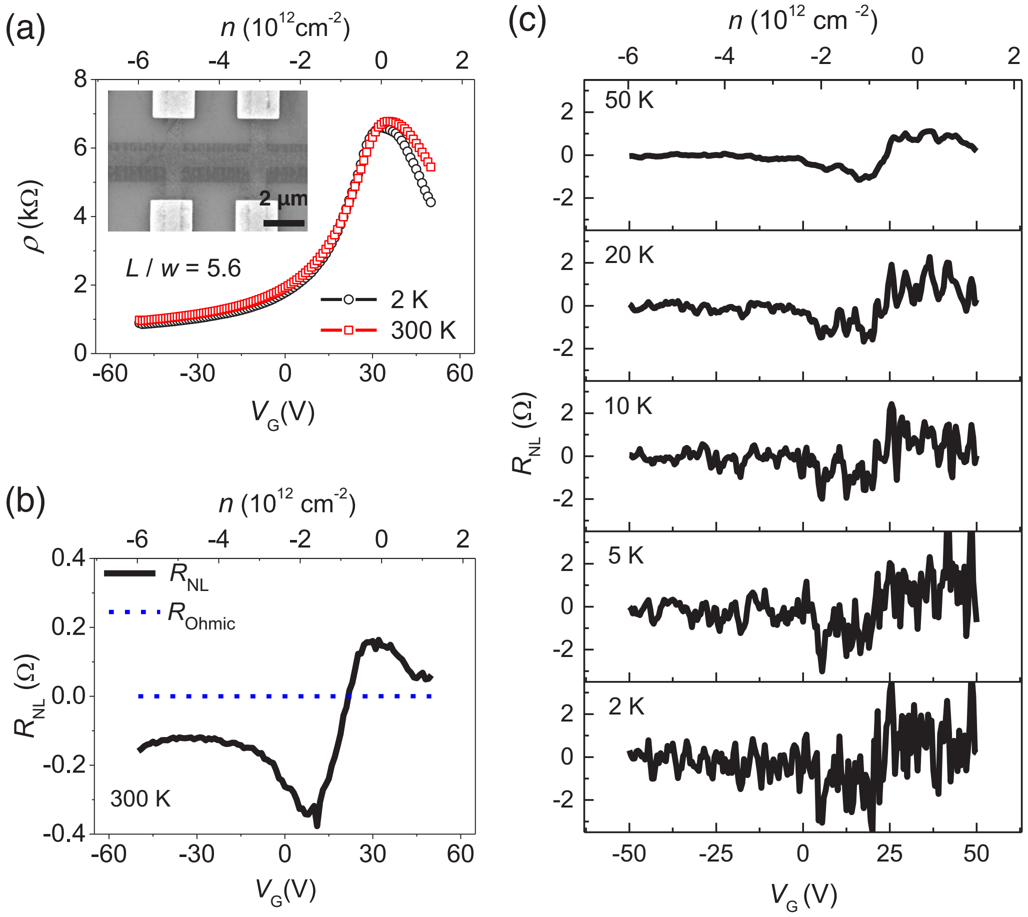

FIG. 2. The local and nonlocal resistance of the Au-clustered graphene device B at various temperatures. (a) Local resistance as a function of applied gate voltage for the Au-clustered device B at $T = 2$ and 300 K. The Dirac point is located at around 33 V. The inset displays a SEM image of device B, which has $L/w = 5.6$. (b) R_{NL} vs V_G of device B at 300 K. The blue dashed line indicates the calculated $R_{\mathrm{NL}}^{\mathrm{Ohm}}$. (c) R_{NL} vs V_{G} of device B at 2, 5, 10, 20, and 50 K.

FET peak near the Dirac point. The current in local probes introduces joule heating and temperature gradient along the central channel line. Then, the thermoelectric voltage given by the Seebeck coefficient can induce offset voltage in nonlocal probes. Because the Seebeck coefficient has an opposite sign for electron and hole majority carriers, it changes sign near the charge neutral point, and so does the subsequent offset voltage in nonlocal probes [30]. This thermoelectric offset voltage is proportional to I^2 (see Supplemental Material [26]). Thus, the nonlocal I-V curves originated from such a thermal effect should display quadratic behavior (see Supplemental Material [26]).

The R_{NL}s of device B as lowering temperature are displayed in Fig. 2(c). A significant fluctuation in R_{NL} can be observed. And this fluctuation becomes stronger with lowering temperature. We note that recent theoretical simulation of θ_{SH} in graphene with Au adatoms and/or clusters also showed a gate-dependent fluctuation [24]. In general, conductance fluctuations in graphene can also occur at low temperature due to the quantum interference of carriers, which is largest near the Dirac point due to the presence of random electron and hole puddles [31,32]. The quantum interference of spins in graphene can also induce a large gate-dependent fluctuation [33]. Because conductance fluctuations are dependent on variations in Fermi energy, gate-dependent R_{NL}s, especially at 2 K and 5 K [Fig. 2(b)] display similar fluctuation pattern. Thus, the observed gate-dependent fluctuation in R_{NL} is likely associated with the fluctuation in both θ_{SH} and conductance fluctuation. In short, the observed gate-dependent R_{NL} could be a consequence of entangled $R_{\mathrm{NL}}^{\mathrm{Thermal}}$, $R_{\mathrm{NL}}^{\mathrm{SHE}}$, and conductance fluctuations.

B. Gate-dependent spin Hall induced nonlocal resistance in Au-clustered graphene

An effective method to determine $R_{\mathrm{NL}}^{\mathrm{SHE}}$ is to examine the spin precession signature. Here, the SHE induces a spin current along the bridging channel with a polarization perpendicular to the plane. Thus, the in-plane magnetic field causes the Larmor precession of carriers' spins [4,8]. This nonmonotonic oscillatory signal can be fitted with [34]

$$R_{\mathrm{NL}}^{\mathrm{SHE}} = \tfrac{1}{2}\theta_{\mathrm{SH}}^{2}\rho w \mathrm{Re}[(\sqrt{1+i\omega_{\mathrm{B}}\tau_{\mathrm{s}}}/\lambda_{\mathrm{s}})e^{-(\sqrt{1+i\omega_{\mathrm{B}}\tau_{\mathrm{s}}}/\lambda_{\mathrm{s}})L}], \qquad (1)$$

where θ_{SH} is the spin hall angle, τ_s is the spin relaxation time, and λ_s is the spin relaxation length. $\omega_B = \Gamma B_{\parallel}$ is the Larmor frequency, Γ is the gyromagnetic ratio, and $B_{\parallel}$ is the applied in-plane magnetic field. The in-plane field-dependent R_{NL} for various gate voltages at 2 K is displayed in Figs. 3(a)–3(d). The

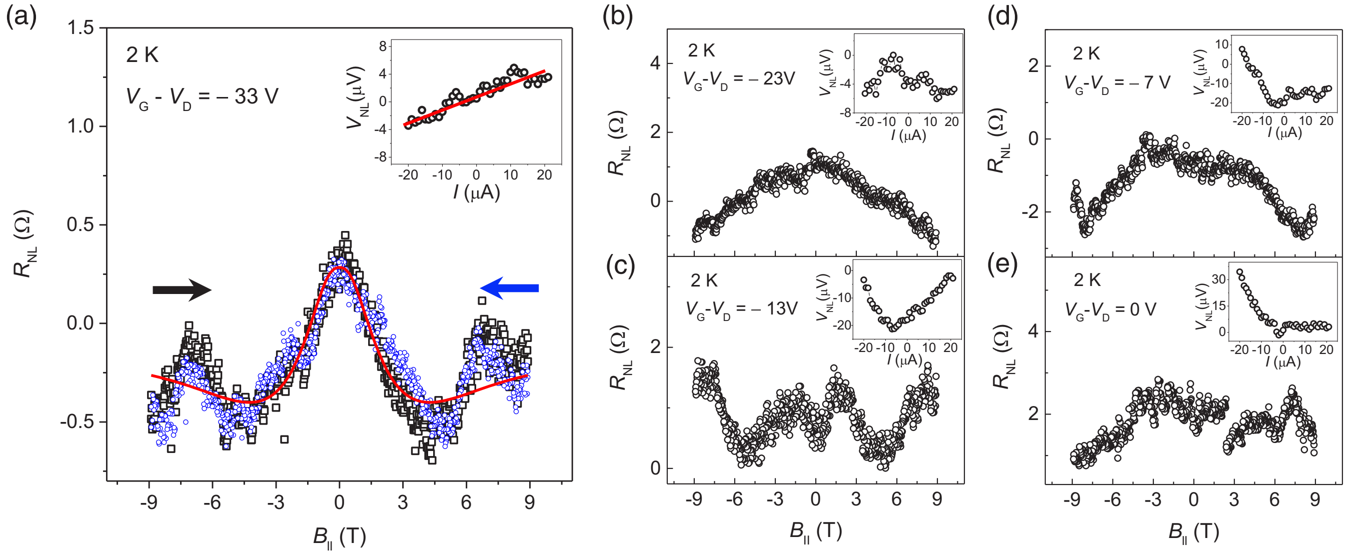

FIG. 3. Gate voltage dependence of $R_{\rm NL}$ vs $B_\parallel$ curves measured for device B. (a) $R_{\rm NL}$ vs $B_\parallel$ of device B at $T = 2$ K measured at $V_{\rm G} - V_{\rm D} = -33$ V. The red line is a fitting curve with Eq. (1). Black and blue symbols are data measured during negative-to-positive and positive-to-negative field scans, respectively. The inset displays nonlocal I-V curves. The red line in the inset is a linear fit. (b)–(e) $R_{\rm NL}$ vs $B_\parallel$ of device B at $T = 2$ K measured at various $V_{\rm G} - V_{\rm D} = -23, -13, -7$, and 0 V. The insets display nonlocal I-V curves measured at various applied gate voltages.

insets in Figs. 3(a)–3(d) show the nonlocal I-V curve for each applied gate voltage. Among the various gate voltages, only at $V_{\rm G} - V_{\rm D} = -33$ V, $R_{\rm NL}(B_\parallel)$ exhibits a precession signature similar to that given by Eq. (1). In addition, the nonlocal I-V curve only at $V_{\rm G} - V_{\rm D} = -33$ V exhibits monotonic linear behavior, as predicted in $R_{\rm NL}^{\rm SHE}$. The behaviors of the nonlocal I-V curves at different gate voltages can be interpreted as a combination of the nonlocal signal from various fluctuations and from the thermal effect ($\sim I^2$). Thus, it can be inferred that $R_{\rm NL}^{\rm SHE}$ is dominant at a particular bias of $V_{\rm G} - V_{\rm D} = -33$ V; the field dependent $R_{\rm NL}$ at $V_{\rm G} - V_{\rm D} = -33$ V can be fitted well with Eq. (1). We note that the spin precession signatures of $R_{\rm NL}$ in other fabricated devices also strongly rely on the applied gate voltage (see Supplemental Material [26]). In particular, slight variations in the gate voltage ($\sim$1 V) are enough to suppress the Hanle signature. The absence of the Hanle curve near the charge neutral point and its appearance at a particular gate voltage could be attributed to following reasons. First, the fluctuation of nonlocal resistance could overcast $R_{\rm NL}^{\rm SHE}$ and the Hanle signal. Second, the $\theta_{\rm SH}$ and thus $R_{\rm NL}^{\rm SHE}$ could themselves have significant gate-dependent fluctuation. We note that the Fermi level dependence of the SHE was also found in other Dirac fermionic systems [35]. In order to confirm whether $R_{\rm NL}$ at a particular gate bias ($V_{\rm G} - V_{\rm D} = -33$ V) originates from $R_{\rm NL}^{\rm SHE}$, we further examined field-dependent $R_{\rm NL}$ at various temperatures.

Figure 4(a) shows $R_{\rm NL}(B_\parallel)$ measured at temperatures $T = 2, 5, 10, 20$, and 50 K. All curves exhibit oscillatory signatures with increasing width as the temperature is increased. For the conventional Hanle curve, the width of the curve approximately corresponds to the spin scattering rate (τ_s^{-1}). The broadening of the width with increasing temperature is likely associated with reduced τ_s at higher temperatures. Thus, the observed $R_{\rm NL}(B_\parallel)$ at various temperatures is consistent with the behavior of $R_{\rm NL}^{\rm SHE}$. The red lines in Fig. 4(a) are fits of Eq. (1) to the measured data. At 2 K, the estimated parameters

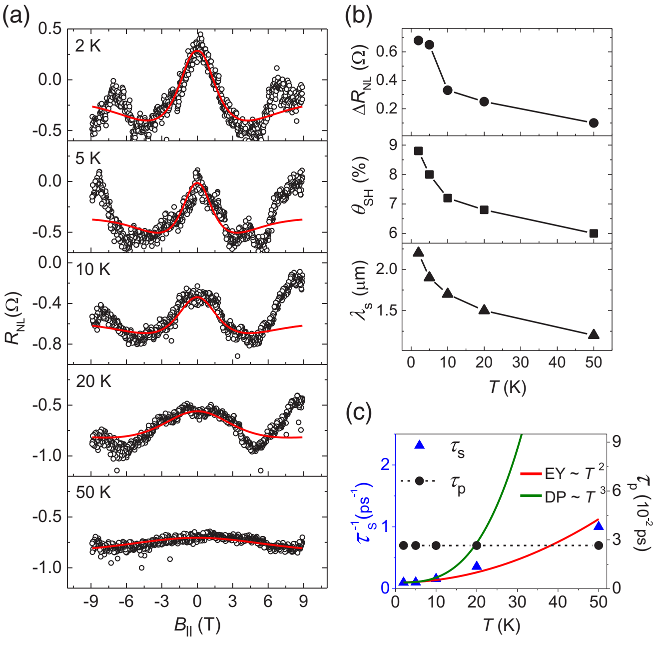

FIG. 4. Temperature dependence of $R_{\rm NL}(B_\parallel)$ and τ_s measured for device B. (a) $R_{\rm NL}$ vs $B_\parallel$ of device B measured at $V_g - V_{\rm D} = -33$ V for various temperatures (2, 5, 10, 20, and 50 K). The red lines are fits of Eq. (1) to the measured $R_{\rm NL}$s. (b) Temperature dependence of the parameters extracted from fitting with Eq. (1). $\Delta R_{\rm NL}$, $\theta_{\rm SH}$, and λ_s are displayed from top to bottom. (c) Temperature dependence of τ_s^{-1} (▲) and τ_p (●). The green and the red line are the predicted temperature dependences for DP and EY spin relaxation mechanisms, respectively.

are $\theta_{\rm SH} \sim 8.8\%$, $t_s \sim 10$ ps, and $\lambda_s \sim 2.2\,\mu$m. Figure 4(b) displays the temperature dependence of the extracted parameters $\Delta R_{\rm NL}$,$\theta_{\rm SH}$, and λ_s obtained by fitting with Eq. (1). All parameters exhibit a general trend of reduction with increasing temperature. One might suspect that the observed $R_{\rm NL}^{\rm SHE}$ and its field dependence originated from the Au bypass. However, the spin in Au could not transport over 5.6 μm, and the observed FET characteristics clearly support that the charge carriers mainly transport through the graphene. We note that this temperature-dependent broadening of the precession signature at a particular gate voltage is consistently observed in our Au-clustered graphene devices (see Supplemental Material [26]). The appearances of the Hanle curve in other devices also accompany with the linear I-V curve at the same gate bias. Figure 4(c) displays the temperature dependence of τ_s^{-1}, which exhibits a nonlinear increase with temperature. Conversely, τ_p obtained from the FET results is nearly independent of temperature, as shown in Fig. 4(c). This implies that the charged impurities in our studied sample introduce considerable Coulomb scattering, which prevails over phonon scattering even at relatively high temperature [27,36]. In contrast to τ_p,τ_s in graphene is expected to have a strong temperature dependence [5]. The two main processes attributed to the spin relaxation in graphene are D'yakonov-Perel' (DP) [37] and EY [38,39] mechanisms. Within the DP mechanism originated from a broken inversion symmetry, τ_s^{-1} is inversely proportional to τ_p^{-1} and proportional to T^3, leading to the relation $\tau_{s,\rm DP}^{-1} \propto T^3\,\tau_p$ [40]. For the EY mechanism, τ_s^{-1} is directly proportional to τ_p^{-1} and T^2, as given by $\tau_{s,EY}^{-1} \propto T^2\,\tau_p^{-1}$ [40]. If τ_p is independent of temperature, then τ_s^{-1} of either the DP or EY mechanism should be proportional to T^3 or T^2, respectively. Our results show that τ_s^{-1} is proportional to T^2, indicating that EY spin relaxation prevails over DP spin relaxation. These results thus suggest that the observed $R_{\rm NL}^{\rm SHE}$ in our device is likely induced by the spin charge conversion from the extrinsic SHE. When EY spin relaxation is dominant, the strength of SOC can be inferred from $\Delta_{\rm SOC} = \varepsilon_{\rm F}\sqrt{\tau_{\rm p}/\tau_{\rm s}}$ [8,41,42], where $\varepsilon_{\rm F}$ is the Fermi energy given by $\varepsilon_{\rm F} = \hbar v_{\rm F} k_{\rm F} = \hbar v_{\rm F}\sqrt{\pi n}$. At $V_{\rm G}-V_{\rm D} = -33$ V($n = 2.37 \times 10^{12}$ cm^{-2}), $\Delta_{\rm SOC} \approx 9.0$ meV. The spin diffusion coefficient $D_{\rm s} = \lambda_{\rm s}^2/\tau_{\rm s}$ is estimated to be $\sim$0.5 m^2 s^{-1} at 2 K, and this value is about 10 times larger than $D_{\rm c} = v_{\rm F}^2\tau_{\rm p}$. We note that this inequality of $D_{\rm s} \neq D_{\rm c}$ is often found in low-dimensional systems [43].

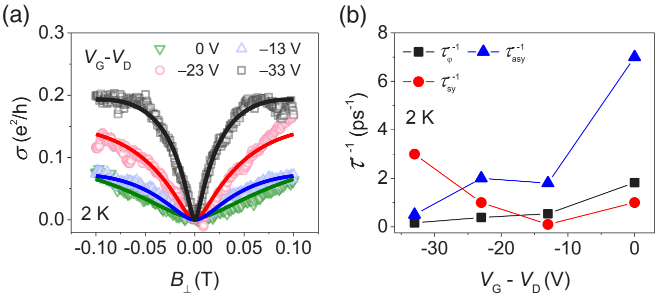

FIG. 5. Gate voltage dependence of MC and the symmetry of the SOS rate. (a) The MC of the Au-clustered graphene device at 2 K measured for various gate voltages ($V_{\rm G} - V_{\rm D} = -33, -23, -13$, and 0 V). All curves display a WL behavior. The solid lines are fits of Eq. (2) to the measured data. (b) Gate dependence of the extracted τ_φ^{-1}, $\tau_{\rm sy}^{-1}$, and $\tau_{\rm asy}^{-1}$.

C. The MC and the symmetry of SOC in Au-clustered graphene

The spin relaxation mechanisms can be further studied through the quantum interference effect on the diffusive transport [44–46]. The presence of SOC affects the phase coherence of electrons, leading to reduced weak localization (WL) or even weak antilocalization (WAL). A recent theoretical study showed that the symmetry of SOC in graphene can also be inferred from MC [44]. Here, we further investigate the symmetry of SOC in Au-clustered graphene. According to Ref. [44], asymmetric SOC causes DP spin relaxation and symmetric SOC induces EY spin relaxation, which leads to the following expression for MC,

$$\Delta\sigma(B) = \frac{e^2}{2\pi h}\left[F\left(\frac{B}{B_\varphi}\right) - F\left(\frac{B}{B_\varphi + B_{\rm asy}}\right) - 2F\left(\frac{B}{B_\varphi + B_{\rm s}}\right)\right]$$

$$B_{{\rm asy,s},\varphi} = \frac{\hbar c}{4De}\tau_{{\rm asy,s},\varphi}^{-1}, \quad F(x) = \ln x + \psi\left(0.5 + \frac{1}{x}\right), \qquad (2)$$

where ψ is the digamma function, $\hbar$ is the Planck constant, τ_φ^{-1} is the inelastic dephasing, and $\tau_{\rm asy}^{-1}$ is the SOS rate associated with asymmetric SOC. The $\tau_{\rm s}^{-1}$ is the total SOS rate, and thus, $\tau_{\rm s}^{-1} = \tau_{\rm asy}^{-1} + \tau_{\rm sy}^{-1}$ (where $\tau_{\rm sy}^{-1}$ is the symmetric SOS rate). The solid lines in Fig. 5(a) are the fits of Eq. (2) to the measured MCs of device B. Similar to previous reports [47], the estimated phase coherence time is in order of 10^{-12} s, which gradually increased as the carrier concentration was increased. Near the charge neutral point ($V_{\rm G} - V_{\rm D} = 0$ V), estimated $\tau_{\rm asy}^{-1}$ and $\tau_{\rm sy}^{-1}$ were 7×10^{12} and 1×10^{12} s^{-1}, respectively. In contrast, estimated $\tau_{\rm asy}^{-1}$ and $\tau_{\rm sy}^{-1}$ at $V_{\rm G} - V_{\rm D} = -33$ V were 5×10^{11} and 3×10^{12} s^{-1}, respectively. Thus, asymmetric SOS prevails near the charge neutral point, which is gradually reduced as the concentration is increased. At $V_{\rm G} - V_{\rm D} = -33$ V, the ratio of $\tau_{\rm sy}^{-1}/\tau_{\rm s}^{-1}$ was $\sim$85% [Fig. 5(b)]. This dominance of symmetric SOS leads to EY spin relaxation rather than DP spin relaxation at higher carrier concentrations. This result is consistent with the spin relaxation mechanism deduced from the temperature-dependent behavior of the measured $R_{\rm NL}^{\rm SHE}$. Here, the estimated $\tau_{\rm s}$ using WL/WAL theory is much shorter than that obtained from nonlocal measurements. We note that the estimation of $\tau_{\rm s}$ using WL/WAL theory typically produces reduced lifetime by one order of magnitude, as studied elsewhere [46].

IV. CONCLUSION

In conclusion, we showed the generation of a spin current by the spin Hall effect, nonlocal spin diffusion, and the spin detection by the inverse SHE in Au-clustered graphene hall bar device. The observed nonlocal resistance exhibits significant fluctuation with applied gate voltage, which is likely due in part to conductance fluctuation and spin Hall angle fluctuation. The dominance of SHE induced nonlocal resistance was observed at particular carrier concentration, which was further confirmed through the Hanle curve and its temperature dependence. The behavior of $\tau_s(T)$ obtained from Hanle curves is consistent with the determined SOC symmetry, which is asymmetric near the Dirac point and symmetric at higher concentrations. Our results inspire an alternative route for generating and detecting spin currents in graphene and provide important insights for the SHE as well as the symmetry of SOC in physically decorated graphene.

ACKNOWLEDGMENTS

This paper was supported by the National Research Foundation of Korea (NRF) (South Korea) (Grants No. 2014R1A1A2055685, No. 2016R1D1A1B03935019, and No. 2012M3A9C6049797) and Future Challenge Project or Creativity and Innovation Project (No. 1.140092.01) funded by the Ulsan National Institute of Science and Technology (South Korea).

---

[1] A. H. Castro Neto, F. Guinea, N. M. R. Peres, K. S. Novoselov, and A. K. Geim, Rev. Mod. Phys. **81**, 109 (2009).

[2] A. K. Geim and K. S. Novoselov, Nat. Mater. **6**, 183 (2007).

[3] R. V. Gorbachev, J. C. W. Song, G. L. Yu, A. V. Kretinin, F. Withers, Y. Cao, A. Mishchenko, I. V. Grigorieva, K. S. Novoselov, L. S. Levitov, and A. K. Geim, Science **346**, 448 (2014).

[4] N. Tombros, C. Jozsa, M. Popinciuc, H. T. Jonkman, and B. J. van Wees, Nature **448**, 571 (2007).

[5] W. Han and R. K. Kawakami, Phys. Rev. Lett. **107**, 047207 (2011).

[6] W. Han, R. K. Kawakami, M. Gmitra, and J. Fabian, Nat. Nanotechnol. **9**, 794 (2014).

[7] J. Sinova, S. O. Valenzuela, J. Wunderlich, C. H. Back, and T. Jungwirth, Rev. Mod. Phys. **87**, 1213 (2015).

[8] J. Balakrishnan, G. K. W. Koon, M. Jaiswal, A. H. C. Neto, and B. Ozyilmaz, Nat. Phys. **9**, 284 (2013).

[9] S. Datta and B. Das, Appl. Phys. Lett. **56**, 665 (1990).

[10] A. Manchon, H. C. Koo, J. Nitta, S. M. Frolov, and R. A. Duine, Nat. Mater. **14**, 871 (2015).

[11] H. C. Koo, J. H. Kwon, J. Eom, J. Chang, S. H. Han, and M. Johnson, Science **325**, 1515 (2009).

[12] W. Y. Choi, H. J. Kim, J. Chang, S. H. Han, H. C. Koo, and M. Johnson, Nat. Nanotechnol. **10**, 666 (2015).

[13] P. Chuang, S. C. Ho, L. W. Smith, F. Sfigakis, M. Pepper, C. H. Chen, J. C. Fan, J. P. Griffiths, I. Farrer, H. E. Beere, G. A. C. Jones, D. A. Ritchie, and T. M. Chen, Nat. Nanotechnol. **10**, 35 (2015).

[14] M. Gmitra, D. Kochan, and J. Fabian, Phys. Rev. Lett. **110**, 246602 (2013).

[15] S. Irmer, T. Frank, S. Putz, M. Gmitra, D. Kochan, and J. Fabian, Phys. Rev. B **91**, 115141 (2015).

[16] A. Pachoud, A. Ferreira, B. Ozyilmaz, and A. H. Castro Neto, Phys. Rev. B **90**, 035444 (2014).

[17] K. T. Chan, J. B. Neaton, and M. L. Cohen, Phys. Rev. B **77**, 235430 (2008).

[18] D. Marchenko, A. Varykhalov, M. R. Scholz, G. Bihlmayer, E. I. Rashba, A. Rybkin, A. M. Shikin, and O. Rader, Nat. Commun. **3**, 1232 (2012).

[19] J. Balakrishnan, G. K. W. Koon, A. Avsar, Y. Ho, J. H. Lee, M. Jaiswal, S. J. Baeck, J. H. Ahn, A. Ferreira, M. A. Cazalilla, A. H. C. Neto, and B. Ozyilmaz, Nat. Commun. **5**, 4748 (2014).

[20] A. Avsar, J. H. Lee, G. K. W. Koon, and B. Ozyilmaz, 2D Mater. **2**, 044009 (2015).

[21] Z. Z. Jia, B. M. Yan, J. J. Niu, Q. Han, R. Zhu, D. P. Yu, and X. S. Wu, Phys. Rev. B **91**, 085411 (2015).

[22] Y. L. Wang, X. H. Cai, J. Reutt-Robey, and M. S. Fuhrer, Phys. Rev. B **92**, 161411 (2015).

[23] A. A. Kaverzin and B. J. van Wees, Phys. Rev. B **91**, 165412 (2015).

[24] D. Van Tuan, J. M. Marmolejo-Tejada, X. Waintal, B. K. Nikolic, S. O. Valenzuela, and S. Roche, Phys. Rev. Lett. **117**, 176602 (2016).

[25] H. D. Yun, J. Kwak, S. Y. Kim, H. Seo, I. C. Bang, S. Y. Kim, S. Kang, and S. Y. Kwon, J. Alloy Compd. **675**, 37 (2016).

[26] See Supplemental Material at http://link.aps.org/supplemental/10.1103/PhysRevB.95.245414 for details regarding further material characterization, Au coverage on graphene, comparison on WL between as-grown and Au-clustered CVD graphene, thermoelectric nonlocal resistance behavior, and reproducibility of gate-dependent nonlocal spin resistance.

[27] J. H. Chen, C. Jang, S. Adam, M. S. Fuhrer, E. D. Williams, and M. Ishigami, Nat. Phys. **4**, 377 (2008).

[28] G. Mihajlovic, J. E. Pearson, M. A. Garcia, S. D. Bader, and A. Hoffmann, Phys. Rev. Lett. **103**, 166601 (2009).

[29] D. A. Abanin, S. V. Morozov, L. A. Ponomarenko, R. V. Gorbachev, A. S. Mayorov, M. I. Katsnelson, K. Watanabe, T. Taniguchi, K. S. Novoselov, L. S. Levitov, and A. K. Geim, Science **332**, 328 (2011).

[30] J. Renard, M. Studer, and J. A. Folk, Phys. Rev. Lett. **112**, 116601 (2014).

[31] A. N. Pal, V. Kochat, and A. Ghosh, Phys. Rev. Lett. **109**, 196601 (2012).

[32] C. Ojeda-Aristizabal, M. Monteverde, R. Weil, M. Ferrier, S. Gueron, and H. Bouchiat, Phys. Rev. Lett. **104**, 186802 (2010).

[33] M. H. D. Guimaraes, P. J. Zomer, I. J. Vera-Marun, and B. J. van Wees, Nano Lett. **14**, 2952 (2014).

[34] D. A. Abanin, A. V. Shytov, L. S. Levitov, and B. I. Halperin, Phys. Rev. B **79**, 035304 (2009).

[35] K. Kondou, R. Yoshimi, A. Tsukazaki, Y. Fukuma, J. Matsuno, K. S. Takahashi, M. Kawasaki, Y. Tokura, and Y. Otani, Nat. Phys. **12**, 1027 (2016).

[36] J. H. Chen, C. Jang, S. D. Xiao, M. Ishigami, and M. S. Fuhrer, Nat. Nanotechnol. **3**, 206 (2008).

[37] M. I. Dyakonov and V. I. Perel, Sov. Phys. Solid State **13**, 3023 (1972).
[38] R. J. Elliott, Phys. Rev. **96**, 266 (1954).
[39] Y. Yafet, in *Solid State Physics*, edited by F. Seitz and D. Turnbull (Academic, New York, 1963), Vol. 14, p. 1.
[40] S. Bandyopadhyay and M. Cahay, *Introduction to Spintronics* (CRC Press, Boca Raton, Florida, 2008).
[41] D. Huertas-Hernando, F. Guinea, and A. Brataas, Phys. Rev. Lett. **103**, 146801 (2009).
[42] H. Ochoa, A. H. Castro Neto, and F. Guinea, Phys. Rev. Lett. **108**, 206808 (2012).
[43] S. Pramanik, S. Bandyopadhyay, and M. Cahay, J. Appl. Phys. **104**, 014304 (2008).
[44] E. McCann and V. I. Fal'ko, Phys. Rev. Lett. **108**, 166606 (2012).
[45] Z. Wang, D. K. Ki, H. Chen, H. Berger, A. H. MacDonald, and A. F. Morpurgo, Nat. Commun. **6**, 8339 (2015).
[46] Z. Wang, D.-K. Ki, J. Y. Khoo, D. Mauro, H. Berger, L. S. Levitov, and A. F. Morpurgo, Phys. Rev. X **6**, 041020 (2016).
[47] F. V. Tikhonenko, A. A. Kozikov, A. K. Savchenko, and R. V. Gorbachev, Phys. Rev. Lett. **103**, 226801 (2009).